Physical Sciences - Daytona Beach   College of Arts & Sciences

2003

Measurements of Atmospheric Stability in the Mesopause Region at Starfire Optical Range, NM

Yucheng Zhao
Utah State University

Alan Z. Liu
Embry Riddle Aeronautical University - Daytona Beach, liuz2@erau.edu

Chester S. Gardner
University of Illinois at Urbana-Champaign

Follow this and additional works at: https://commons.erau.edu/db-physical-sciences

Part of the Physical Sciences and Mathematics Commons

Measurements of atmospheric stability in the mesopause region at starfire optical range, NM

Yucheng Zhao[a], Alan Z. Liu[b,*], Chester S. Gardner[b]

[a]*Utah State University, Logan, Utah, USA*

[b]*Departments of Electrical & Computer Engineering, University of Illinois at Urbana-Champaign, Electro-Opt Lab, 308 CSRL, MC-229, 1308 West Main Street, Urbana, IL 61801 USA*

Abstract

The structure and seasonal variations of static (convective) and dynamic (shear) instabilities in the mesopause region (80–105 km) are examined using high-resolution wind and temperature data obtained with a Na lidar at the Starfire Optical Range, NM. The probabilities of static and dynamic instability are sensitive functions of $\overline{N^2/S^2}$, where N is the buoyancy frequency and S is the total vertical shear in the horizontal winds. The mesopause region is most stable in summer when the mesopause is low, N is large and S is small. Monthly mean $\overline{N^2/S^2}$ varies from a maximum value of about 1.06 in mid-summer to a minimum of 0.68 in January. The annual mean values of N and S are, respectively, $0.021\,\mathrm{s}^{-1}$ and $23\,\mathrm{ms}^{-1}\,\mathrm{km}^{-1}$. The probabilities of static and dynamic instabilities are maximum in mid-winter when they average about 10% and 12%, respectively, and are minimum in summer when they average about 7% and 5%, respectively. The observations are generally consistent with theoretical predictions based on Gaussian models for the temperature and wind fluctuations induced by gravity waves. They also show that statically unstable conditions are generally preceded by dynamically unstable conditions. The instability probabilities vary considerably from night to night and the structure of the unstable regions are significantly influenced by atmospheric tides. Tides alone are usually not strong enough to induce instability but they can establish the environment for instabilities to develop. As the tidal temperature perturbations propagate downward, they reduce the stability on the topside of the positive temperature perturbation. Instabilities are then induced as gravity waves propagate through this layer of reduced static stability.
© 2002 Elsevier Science Ltd. All rights reserved.

1. Introduction

It has long been recognized that gravity wave saturation and dissipation processes play a dominant role in maintaining the general circulation of the middle atmosphere. Dissipating waves transport heat, horizontal momentum, and constituents and through such processes have a profound effect on middle atmosphere structure and composition. A number of theories invoking different physical mechanisms have been developed to explain the gravity wave dissipation process (Hodges, 1967; Lindzen, 1981; Weinstock, 1990; Dewan and Good, 1986; Dunkerton, 1987; Hines, 1991; Gardner, 1994). According to the linear saturation theory, shear (dynamic) and convective (static) instabilities control wave dissipation (Hodges, 1967; Dewan and Good, 1986). When the wave amplitude reaches a critical value, the atmosphere becomes locally unstable, the wave begins to break and dissipates its energy by generating turbulence. This dissipation mechanism is believed to be one of the main sources of turbulence in the middle atmosphere. The turbulence, in turn, further limits the growth of gravity wave amplitudes.

Till now, most studies of the instability properties in the mesopause region between 80 and 105 km have been limited to theoretical work, numerical simulations, and

* Corresponding author. Tel.: +217-333-6982; fax: +217-333-4303.

E-mail address: liuzr@uiuc.edu (A.Z. Liu).

laboratory experiments (e.g. Fritts et al., 1994; Koop and McGee, 1986). Measuring stability properties of the atmosphere in the presence of gravity waves requires high temporal and spatial resolution wind and temperature data. It is necessary to resolve the important waves, which can have periods as small as a few minutes, and vertical wavelengths as small as a few kilometers. Observational studies of dynamic and static instabilities are mostly limited to the stratosphere and lower mesosphere using balloon and Rayleigh lidar observations (Sica and Thorsley, 1996; Allen and Vincent, 1995; Pfenninger et al., 1999). During the past 10 years, several campaigns have been conducted to characterize shear and convective instabilities in the mesopause region in order to understand the turbulence structure (e.g., MAC/EPSILON conducted in 1987, Blix et al., 1990; DYANA conducted in 1990, Offermann, 1994; Lübken et al., 1994).

In this paper we report observations and analysis of both static and dynamic instabilities in the mesopause region using data obtained with a Na wind/temperature lidar. The Na lidar can measure wind and temperature profiles at high temporal and spatial resolution with relatively small uncertainties. We report 195 h of observations obtained during 32 nights since June of 1998 at the Starfire Optical Range (SOR), near Albuquerque, NM. The data are distributed throughout the year, enabling us to characterize various properties of atmospheric stability, including the seasonal variations. In the next section, we discuss the general characteristics of static and dynamic instabilities, and the effects of gravity waves. We also discuss the observational challenges in measuring instabilities in the mesopause region. In Section 3 we give a brief description of the experiment and instrumentation, followed by the techniques used in processing the data. The observed static and dynamic instabilities, their probabilities, and their seasonal variations are presented in Section 4. The results are summarized in Section 5.

2. Atmospheric stability

The convective or static stability of the atmosphere is characterized by the square of the buoyancy frequency N defined as (Emanuel, 1994)

$$N^2 = \frac{g}{T}\left(\frac{\partial T}{\partial z} + \frac{g}{C_p}\right), \tag{1}$$

where g is the gravitational acceleration (9.5 m s^{-2} in the mesopause region), T is the atmospheric temperature, and $C_p = 1004$ J K^{-1} kg^{-1} is the specific heat at constant pressure. When N^2 is positive, the atmosphere is statically stable. An air parcel displaced adiabatically tends to return to its equilibrium position. Perturbations are suppressed when the atmosphere is statically stable. When N^2 is negative, i.e. when the atmospheric lapse rate $\Gamma = -\partial T/\partial z$ is larger

than the adiabatic lapse rate $g/C_p \approx 9.5$ K km^{-1}, the atmosphere is unstable. Under this condition, an air parcel displaced vertically will tend to continue moving away from its equilibrium position. Small perturbations can develop and be amplified in an unstable atmosphere.

Shear or dynamic instability is induced by large vertical shears of the horizontal wind in combination with low static stability. Dynamic stability is characterized by the Richardson number, Ri, which is defined as (Kundu and Pijush, 1990)

$$Ri = \frac{N^2}{(\partial u/\partial z)^2 + (\partial v/\partial z)^2} = \frac{N^2}{S^2}, \tag{2}$$

where u and v are the zonal and meridional wind profiles, respectively, and $S = [(\partial u/\partial z)^2 + (\partial v/\partial z)^2]^{1/2}$ is the total vertical shear of horizontal wind. Generally, the atmosphere is considered to be dynamically unstable when $0 < Ri < \frac{1}{4}$ (Rohr et al., 1988). Dynamic instability occurs when there is a strong wind shear and/or small static stability. Hodges (1967) pointed out that for the mean atmosphere without gravity waves, it is unlikely for the condition of dynamic instability to be satisfied. But in the presence of gravity waves, large vertical shears of the temperature and horizontal wind can be generated, which often results in thin layers of instability. This effect is most significant above 80 km in the mesopause region where the wave amplitudes can become very large.

Although it is well recognized that static and dynamic instabilities are important wave saturation mechanisms in the mesopause region, a detailed understanding of the stability of this region is still unclear due to the difficulties in obtaining temperature and wind data with sufficient spatial and temporal resolution and accuracy. The buoyancy period is about 5 min at mesopause heights and the viscous dissipation limit is about 1 km (Hines, 1974; Gardner, 1994) so that the smallest scale waves have intrinsic periods near 5 min and vertical wavelengths near 1 km. Therefore to capture most gravity wave effects, at least 500-m vertical resolution and 2.5-min temporal resolution are necessary. Because N^2 and Ri depend on $\partial T/\partial z$ and $S = [(\partial u/\partial z)^2 + (\partial v/\partial z)^2]^{1/2}$, the temperature and wind profiles must be measured with great accuracy so that noise in the data does not bias the stability calculations. If Δz is the vertical resolution, the rms measurement errors in the temperature and horizontal wind must satisfy the following criteria:

$$\Delta T_{\rm rms} \ll \Delta z \, {\rm std}(\partial T'/\partial z)/\sqrt{2} \approx 3 \text{ K}, \tag{3}$$

$$\Delta u_{\rm rms} \ll \Delta z \sqrt{\overline{S^2}}/2 \approx 6 \text{ m s}^{-1}, \tag{4}$$

where "std" is the standard deviation, and we have used 500 m for the resolution and the mean observed values for the rms temperature lapse rate (7.7 K/km) and total wind shear (23 m/s/km). These accuracy and resolution criteria present considerable observational challenges.

By employing high laser powers and large telescopes, Na lidar techniques can obtain wind and temperature data with sufficient resolution and accuracy to observe static and dynamic instabilities between about 80 and 105 km depending on the signal level and Na density. Because both temperature and wind observations are required, the measurement of dynamic instability is considerably more challenging than measuring static instability. Ideally to measure the Richardson number, both the temperature and horizontal winds should be measured simultaneously at the same location. Na lidars can measure temperature and one radial component of the wind field at the same time and the same location. They cannot measure both zonal and meridional wind components simultaneously with temperature or at the same location. Thus, Na lidar has limitations for observing dynamic instabilities.

3. Experimental configuration and data processing

The observations reported here were made with a Na wind/temperature lidar at the SOR located on the Kirtland AFB ($35°$N, $106.5°$W, 1.85 km altitude), near Albuquerque, NM. The facility is operated by the Air Force Research Laboratory, Directed Energy Directorate and includes a 3.5-m astronomical telescope. The University of Illinois Na wind/temperature lidar is coupled to this telescope through the coude optics so that the beam can be pointed at any direction above the horizon. A 1-m diameter portion of the telescope primary mirror is used to project the laser beam while the remainder is used for collecting the backscattered light and focusing it onto the detector. The beam divergence is approximately 1 mrad. At 100 km range, the beam diameter (full width @ e^{-2}) is 100 m. The lidar operates at 30 pulse-per-second and the laser output power varies between 1 and 1.5 W. The power-aperture product varies between 10 and 14 Wm^2 depending on laser power. In this configuration, temperature and radial wind can be measured along the laser beam. Typically the lidar is pointed at zenith (Z) and $10°$ off-zenith to the north (N), south (S), east (E) and west (W) in the following sequence ZNEZSW. At each position, backscatter profiles are obtained with a 90-s integration time and 24-m range resolution. Approximately 30 s are required to point the telescope to the next position. This 6-position sequence is completed about every 12 min so the complete wind and temperature field can be derived every 6 min. To increase signal to noise ratio, the raw wind and temperature data are derived at a spatial resolution of 96 m. The temperature and wind are then binned to 500 m to further reduce the uncertainty due to photon noise. The rms temperature error with this resolution is about 1.5 K between 92.5 ± 7.5 km, just small enough to give a good estimate of N^2.

Zonal (u) and meridional (v) components of the horizontal wind are calculated from radial winds measured at the off-zenith positions. The radial wind is related to the horizontal wind as follows:

$$V_{\mathrm{E}} = u \sin \theta + w \cos \theta, \tag{5}$$

$$V_{\mathrm{W}} = -u \sin \theta + w \cos \theta, \tag{6}$$

$$V_{\mathrm{N}} = v \sin \theta + w \cos \theta, \tag{7}$$

$$V_{\mathrm{S}} = -v \sin \theta + w \cos \theta, \tag{8}$$

where $V_{\mathrm{E}}, V_{\mathrm{W}}, V_{\mathrm{N}}$, and V_{S} are radial winds measured at east, west, north, and south positions, respectively, and w is the vertical wind. $\theta = 10°$ is the zenith angle. Ideally, the horizontal wind u and v could be calculated from Eqs. (5)–(8) if the zenith and off-zenith winds are obtained at the same time and same location. However, it requires about 2 min to make a measurement and move the telescope to the next position. There is also a 15-km spatial difference between the zenith and off-zenith measurements at 90 km altitude and about 22-km difference between north and east or south and west observations. Since the vertical wind w is generally much smaller than the horizontal wind and comparable to the radial wind measurement error, we calculate the horizontal wind by ignoring w in Eqs. (5)–(8). For example, the zonal wind at the east position was simply calculated as

$$u = V_{\mathrm{E}} / \sin \theta. \tag{9}$$

The error of the zonal wind u calculated according to Eq. (9) is

$$\Delta u_{\mathrm{rms}} = \frac{\sqrt{\Delta V_{\mathrm{rms}}^2 + w_{\mathrm{rms}}^2 \cos^2 \theta}}{\sin \theta}, \tag{10}$$

where ΔV_{rms} is the radial wind measurement error and w_{rms} is the rms vertical wind velocity.

For 500-m vertical resolution and 1.5 min integration time, the average radial wind error is about 1.5 m s^{-1} and $w_{\mathrm{rms}} \approx 2.1$ m s^{-1}, corresponding to an error of 14.7 m s^{-1} in horizontal wind. This error is too large to obtain a reliable estimate of Ri. To reduce this error, the vertical resolution is reduced to 1 km, and the horizontal wind and temperature are averaged over two cycles of the 6-position sequence, which spans about 24 min, and includes 4 profiles each of u and v and 12 profiles of temperature. By doing this, waves with period less than 48 min, vertical wavelengths shorter than 2 km, and horizontal wavelengths shorter than about 20 km are eliminated. Averaging significantly reduces photon noise as well as vertical wind contamination. Errors in horizontal wind and temperature for this low-resolution data set average about 2 m s^{-1} and 0.2 K between 92.5 ± 7.5 km. In our analysis, the higher resolution temperature data (500 m, 1.5 min) are used to calculate N^2 to assess static stability while the lower resolution wind and temperature data (1 km, 24 min) are used to calculate Ri to assess dynamic stability. The accuracy of the computed values of Ri is further limited by the fact that zonal and meridional winds are measured at different locations and times.
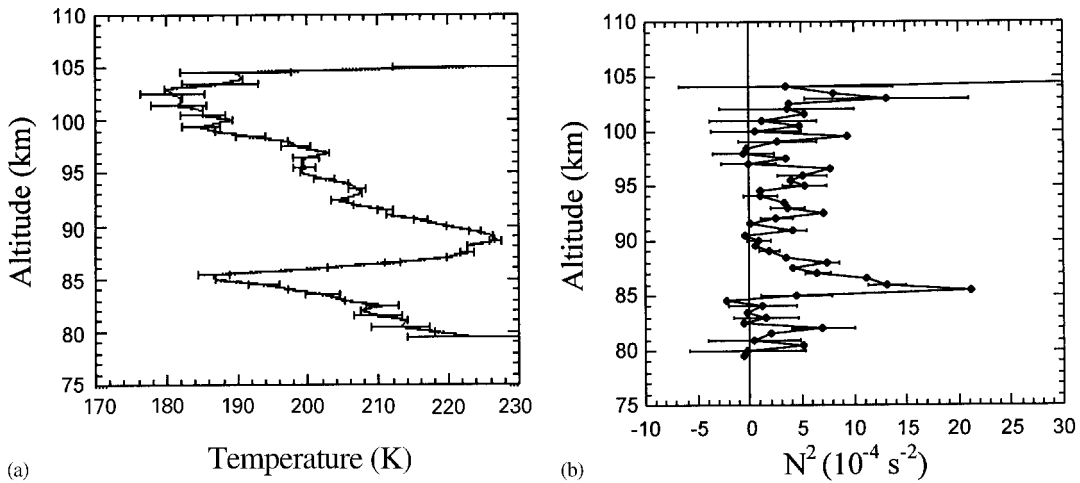
Fig. 1. (a) Temperature and (b) N^2 profiles at 0955 UT on 18 February 1999 with vertical resolution of 500 m. The horizontal bars indicate the errors. The straight vertical line in (b) is the critical value for convective instability. The air is unstable (stable) when the value falls on the left (right) of it.

The probabilities of static and dynamic instabilities are estimated by computing N^2 and Ri at every altitude and time for each night with the respective high and low resolution data discussed above. The relative frequency of the unstable conditions are then determined as the fraction of unstable data points for the entire night. Measurement errors caused by photon noise bias the probabilities computed using this approach. To minimize this bias, we restrict the analysis to that region of the Na layer where the rms measurement error averages less than 1.5 K. Furthermore, the measurement error bias is estimated and subtracted from the measured probability of static instability. The compensation technique is described in Appendix B.

The computed probability of dynamic instability is not compensated for measurement errors. Ri is derived using heavily averaged data with small temperature and wind measurement errors (0.2 K and 2 m s^{-1}). The uncertainties in Ri are dominated by uncertainties associated with the fact that the horizontal winds are measured at different locations separated by about 23 km. These uncertainties are believed to be small, because only gravity waves with horizontal wavelengths larger than about 20 km contribute to the wind and temperature data used to compute Ri.

4. Observations

4.1. Static instabilities

The vertical temperature profile is all that is needed to compute N^2 and identify the statically unstable regions. To illustrate, the temperature profile obtained at 0955 UT on 18 February 1999 is shown in Fig. 1, together with the N^2
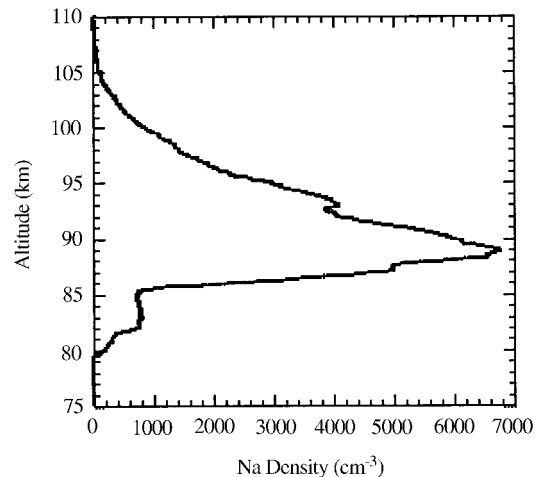

Fig. 2. Na density profile at 0955 UT on 18 February 1999 with vertical resolution of 96 m.

profile calculated from these temperatures. The temperature profile includes wave perturbations with observed periods greater than 3 min and vertical wavelengths greater than 1 km. This resolution captures the effects of most gravity waves expected to be capable of propagating in the mesopause region. Measurement errors are greatest at the bottom and topsides of the Na layer (Fig. 2) where the Na density is smallest, and hence the signal levels are weakest.

Fig. 3a is a plot showing the atmospheric static stability during the night of 18 February 1999. Stable regions are black; unstable regions are colored. Most of the mesopause
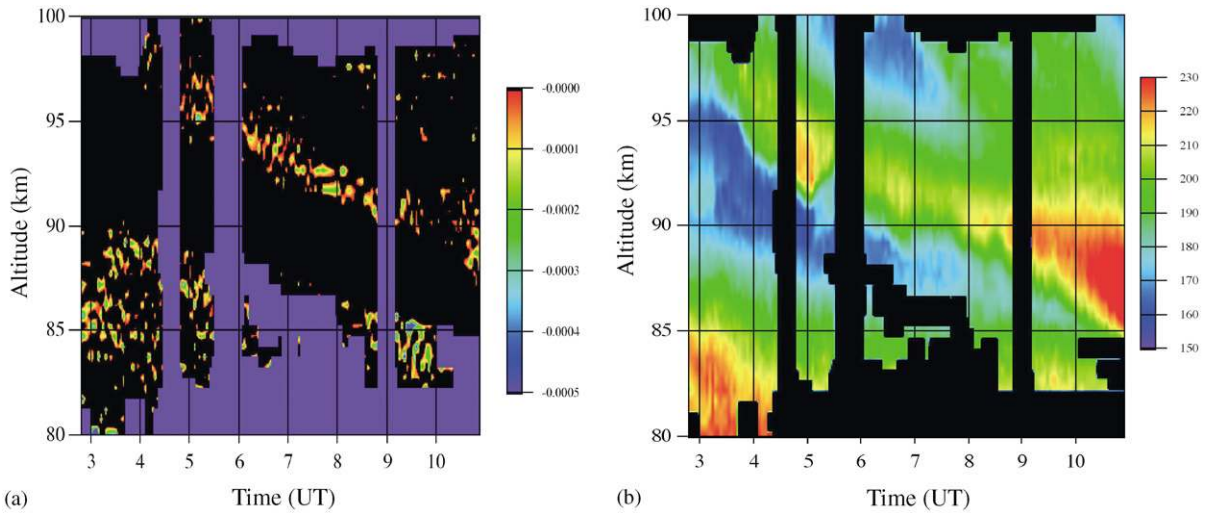
Fig. 3. (a) Convectively unstable regions for 18 February 1999, determined by N^2 calculated from 500-m 1.5-min resolution data. The black region is where $N^2 > 0$; colored region is where $N^2 < 0$. No data is available in purple region. (b) Temperature for the same night.
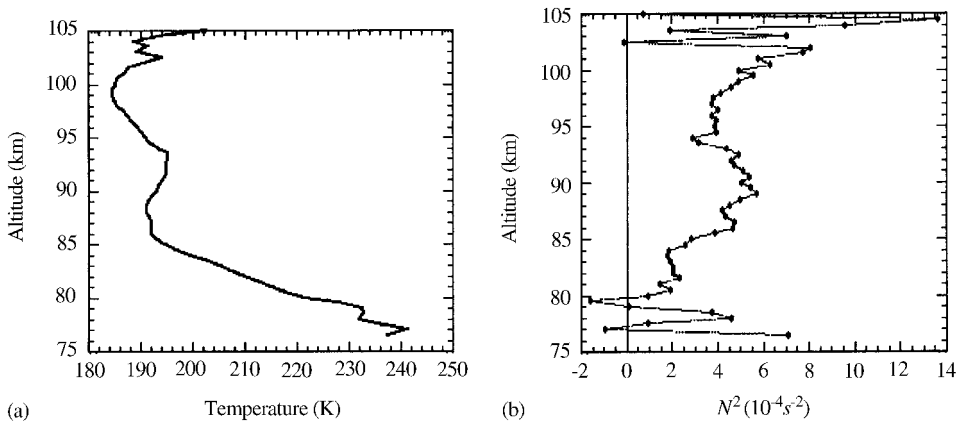

Fig. 4. (a) Nightly mean temperature (zenith only, smoothed by 2 km full-width-half-maximum Hamming window) on 18 February 1999 and (b) $\overline{N^2}$ calculated from (a).

region is stable. There are small unstable regions during the early night below 90 km where the background temperature profile has a large positive lapse rate ($-\partial T/\partial z$). The spatial and temporal scales of these unstable regions are small. From 0400 UT until the end of the observations, an unstable layer propagated downward from 97 km to about 88 km. The thickness of this unstable layer is less than 2 km and it generally persists for about 30 min at a fixed altitude. A plot of the temperature in Fig. 3b shows that there was a large amplitude, downward propagating temperature perturbation associated with the unstable layer. The perturbation is associated with the semi-diurnal tide which has an especially strong thermal amplitude in winter (States and Gardner, 2000). The amplitude can be as large as 10 K, compared with 3 to 4 K for the diurnal tide (States and Gardner, 2000). Fig. 4 shows the nightly mean temperature and $\overline{N^2}$ profile. This mean state is very stable above 90 km, which suggests that the semi-diurnal tide was the main cause of instability on this night. The semi-diurnal tide alone is usually not strong enough to induce instability. However it can establish the environment for instabilities to develop. As the tidal temperature perturbation propagates downward, it reduces the stability on the topside of the positive temperature perturbation. Instabilities are then induced as gravity waves propagate through this layer of reduced static stability.

The probability of static instability was computed for each night of observations and the results are tabulated in Table 1. Other relevant characteristics of the wave activity

Table 1
Observed probabilities of static, dynamic and total instabilities for each night and their annual means. Theoretical means are also listed

Date	$P(N^2 < 0)$ (%)	$P(0 < Ri < \frac{1}{4})$ (%)	$P(Ri < \frac{1}{4})$ (%)
12 Jan. 99	14.2 ± 0.33	12.2	26.4
14 Jan. 99	9.7 ± 0.27	10.1	19.8
15 Jan. 99	4.9 ± 0.58	8.6	13.5
18 Feb. 99	14.1 ± 0.60	18.8	32.9
20 Feb. 99	5.8 ± 1.57	7.5	13.3
16 Apr. 99	8.3 ± 0.42	4.7	13
17 Apr. 99	6.9 ± 0.55	8.8	15.7
18 Apr. 99	7.4 ± 0.70	10.2	17.6
12 May 99	2.7 ± 0.36	3.5	6.2
13 May 99	8.5 ± 0.5	4.2	12.7
14 May 99	7.0 ± 0.61	2.8	9.8
15 May 99	9.8 ± 0.67	13.7	23.5
24 Jun. 98	2.2 ± 0.74	1.5	3.7
26 Jun. 98	8.4 ± 0.71	6.6	15
27 Jun. 98	11.4 ± 0.46	7.2	18.6
12 Aug. 99	7.7 ± 0.60	7.1	14.8
13 Aug. 99	5.4 ± 0.42	6.5	11.9
08 Sep. 99	7.9 ± 1.05	7.3	15.2
09 Sep. 99	7.0 ± 0.41	1.0	8
22 Sep. 98	3.4 ± 0.64	4.3	7.7
24 Sep. 98	7.7 ± 1.04	6.9	14.6
25 Sep. 98	9.2 ± 0.31	3.1	12.3
13 Oct. 99	7.7 ± 0.42	6.4	14.1
15 Oct. 99	9.0 ± 0.34	1.9	10.9
16 Oct. 99	6.8 ± 0.43	9.3	16.1
15 Nov. 98	10.7 ± 0.85	7.6	18.3
16 Nov. 98	5.3 ± 1.98	3.3	8.6
17 Nov. 98	10.6 ± 1.83	10.2	20.8
18 Nov. 98	13.7 ± 2.45	14.6	28.3
17 Dec. 98	7.2 ± 1.07	10.4	17.6
18 Dec. 98	10.1 ± 0.75	8.1	18.2
19 Dec. 98	6.8 ± 0.48	11.9	18.7
Mean	8.0 ± 0.75	7.5	15.5
Theoretical mean	12.1	9.5	21.6

are listed in Table 2. The mean probability of static instability is $8.0 \pm 0.75\%$ with a maximum of $14.2 \pm 0.33\%$ on 12 January 1999 and a minimum of $2.2 \pm 0.74\%$ on 24 June 1998. The annual mean value of $\overline{N^2}$ is 4.45×10^{-4} s^{-2}, which corresponds to a buoyancy period of 4.96 min. $P(N^2 < 0)$ varies from night to night as the gravity wave and tidal activity vary and the background temperature profile changes. Even within the same month, the probability of static instability varies considerably, indicating strong day to day variability in gravity wave and tidal activity.

The monthly mean N^2 and $P(N^2 < 0)$ are plotted versus month in Fig. 5. The mean temperature and N^2 profiles observed during the summer and winter seasons are plotted in Fig. 6. Above the mesopause, the atmosphere is very stable (N^2 is large) because the temperature increases rapidly with increasing altitude. Below the mesopause, the temperature generally decreases with increasing altitude so the atmosphere has a positive lapse rate ($-\partial T/\partial z > 0$) and a smaller $\overline{N^2}$. Since the mesopause is high in winter (~ 100 km) and low in summer (~ 86 km), the mesopause region between 80 and 105 km is less stable in winter (smaller $\overline{N^2}$) than in summer.

The theoretical probability of static stability is derived in Appendix A by assuming that the relative temperature and N^2 perturbations are small and are Gaussian distributed. This theoretical probability of static instability given by Eq. (A.4) is also plotted in Fig. 5 for comparison. Its mean value for all nights is also listed in the last column in Table 1. It was computed using the measured ratios $\overline{N^2}/\sigma_{N^2}$. The predicted probability is larger than observed. We believe this difference is associated with the assumption that N^2 is Gaussian distributed. Fig. 15 in Appendix B is a histogram of the N^2 values measured on 12 January 1999. The distribution is asymmetric and skewed to large positive values of N^2. This effect is associated with gravity wave saturation that limits how deeply the atmosphere can be driven into a statically unstable state. As the atmosphere becomes unstable, the waves begin to saturate and generate turbulence which limits the negative excursions of N^2 and hence the probability of instability. There is no limit for positive excursions of N^2.

4.2. Dynamic instabilities

The horizontal wind and Ri profiles at 0949 UT on 18 February 99 are plotted in Fig. 7. This low resolution data (1 km and 24 min) includes the effects of waves with periods greater than 48 min, vertical wavelengths greater than 2 km, and horizontal wavelengths greater than about 20 km. Although some of the high frequency short vertical scale waves are excluded, this resolution includes the waves responsible for the majority (75%) of the wind shear and temperature lapse rate variances. The data should provide a good characterization of the dynamic instabilities in the mesopause region.

The dynamically unstable regions for 18 February 99 are shown in Fig. 8. The statically unstable regions shown in Fig. 3a are included for comparison. The regions of dynamic instability are also associated with the dominant semidiurnal tide. At a fixed altitude dynamic instabilities tend to occur below and before the static instabilities. This is clearly shown in Fig. 9, which shows the altitudes of maximum total horizontal wind shear and maximum temperature lapse rate for each profile based on the 24-min 1-km data set. At a given altitude, the wind shear reaches its maximum about 1.5 h before the temperature lapse rate reaches its maximum. This time difference is about $\frac{1}{8}$ of the period of the semidiurnal tide. The time lag is due to the phase difference between the temperature and wind perturbations associated with the tide in combination with the background temperature structure. Since N^2 must pass through zero during the

Table 2
Statistical results for each night of observation

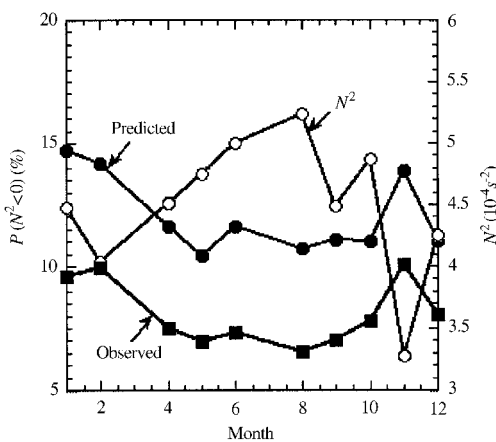| Date	$\overline{N^2}$ $(10^{-4}\ s^{-2})$	$\overline{S^2}$ $(m\ s^{-1}\ km^{-1})^2$	σ_{N^2} $(10^{-4}\ s^{-2})$	$\overline{N^2}/\sigma_{N^2}$	$\sigma_{N^2}/\overline{S^2}$	$\overline{N^2}/\overline{S^2}$
12 Jan. 99	4.03	$(25.6)^2$	4.61	0.87	0.71	0.61
14 Jan. 99	4.75	$(25.0)^2$	4.75	1.00	0.76	0.76
15 Jan. 99	4.64	$(26.6)^2$	3.43	1.35	0.48	0.66
18 Feb. 99	4.19	$(26.1)^2$	4.65	0.90	0.68	0.62
20 Feb. 99	3.88	$(22.4)^2$	2.89	1.34	0.58	0.77
16 Apr. 99	4.63	$(19.6)^2$	4.42	1.05	1.15	1.21
17 Apr. 99	4.46	$(24.0)^2$	3.51	1.27	0.61	0.77
18 Apr. 99	4.45	$(25.7)^2$	3.41	1.30	0.51	0.67
12 May 99	4.95	$(22.4)^2$	3.32	1.49	0.66	0.99
13 May 99	4.37	$(20.6)^2$	3.70	1.18	0.87	1.03
14 May 99	4.73	$(21.6)^2$	3.52	1.34	0.75	1.01
15 May 99	4.94	$(26.8)^2$	4.54	1.09	0.63	0.69
24 Jun. 98	4.91	$(20.8)^2$	3.20	1.53	0.74	1.13
26 Jun. 98	4.90	$(21.6)^2$	4.14	1.18	0.89	1.05
27 Jun. 98	5.20	$(24.2)^2$	5.19	1.00	0.88	0.89
12 Aug. 99	4.90	$(24.4)^2$	4.29	1.14	0.72	0.82
13 Aug. 99	5.59	$(29.8)^2$	4.14	1.35	0.47	0.63
08 Sep. 99	4.01	$(21.6)^2$	3.22	1.25	0.69	0.86
09 Sep. 99	4.28	$(18.7)^2$	3.44	1.24	0.98	1.22
22 Sep. 98	4.80	$(26.1)^2$	3.10	1.55	0.46	0.70
24 Sep. 98	3.90	$(21.3)^2$	3.40	1.15	0.75	0.86
25 Sep. 98	5.50	$(18.9)^2$	5.21	1.06	1.46	1.54
13 Oct. 99	4.38	$(22.5)^2$	3.67	1.19	0.72	0.87
15 Oct. 99	5.39	$(23.5)^2$	4.50	1.20	0.82	0.98
16 Oct. 99	4.84	$(25.3)^2$	3.73	1.30	0.58	0.76
15 Oct. 98	3.50	$(19.9)^2$	3.18	1.10	0.81	0.88
16 Nov. 98	3.30	$(16.3)^2$	2.34	1.41	0.88	1.24
17 Nov. 98	3.21	$(21.9)^2$	2.98	1.08	0.62	0.67
18 Nov. 98	3.08	$(23.2)^2$	3.05	1.01	0.57	0.57
17 Dec. 98	3.83	$(21.5)^2$	3.11	1.23	0.67	0.83
18 Dec. 98	3.95	$(23.2)^2$	3.55	1.11	0.66	0.73
19 Dec. 98	4.96	$(23.3)^2$	3.74	1.33	0.69	0.91
Mean	4.45	$(23.0)^2$	3.81	1.17	0.72	0.84

Fig. 5. Observed monthly mean $\overline{N^2}$ and $P(N^2 < 0)$ along with the $P(N^2 < 0)$ predicted by Eq. (A.4).

transition from a statically stable to unstable condition, Ri will always fall below $\frac{1}{4}$ before N^2 becomes negative (assuming $S \neq 0$). Thus, statically unstable conditions must always be preceded, if only briefly, by dynamically unstable conditions. This does not always occur in Fig. 8 because N^2 and Ri are computed using different resolution data.

$P(0 < Ri < \frac{1}{4})$ and $\overline{S^2}$ were computed for each night and the results are also tabulated in Tables 1 and 2. There is considerable night to night variability in both parameters. The annual mean probability of dynamic instability is 7.5% with a maximum of 18.8% on 18 February 1999 and a minimum of 1.0% on 9 September 1999. The monthly mean values of $\overline{S^2}, \overline{N^2}/\overline{S^2}$, and $P(0 < Ri < \frac{1}{4})$ are plotted in Fig. 10. Also plotted is the theoretical probability given by (A.8) using the measured values of $\overline{N^2}/\sigma_{N^2}$ and $\sigma_{N^2}/\overline{S^2}$. The seasonal variation of $P(0 < Ri < \frac{1}{4})$ is similar to that of $P(N^2 < 0)$. The mesopause region is dynamically more stable in summer (see Fig. 6). This is a result of the larger $\overline{N^2}$ and slightly
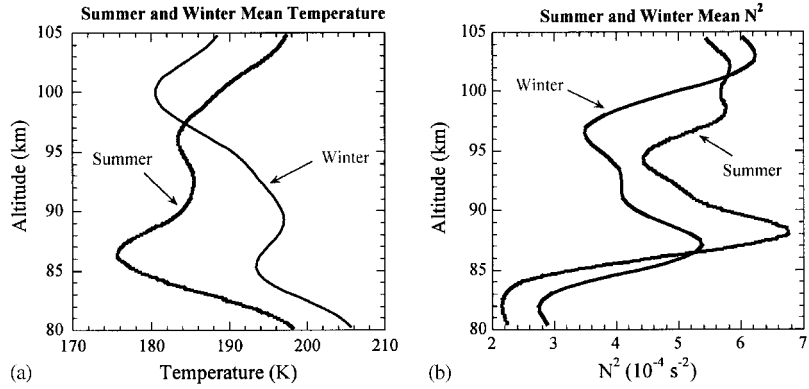
Fig. 6. Mean (a) temperature and (b) N^2 profiles observed during the summer and winter seasons at SOR.
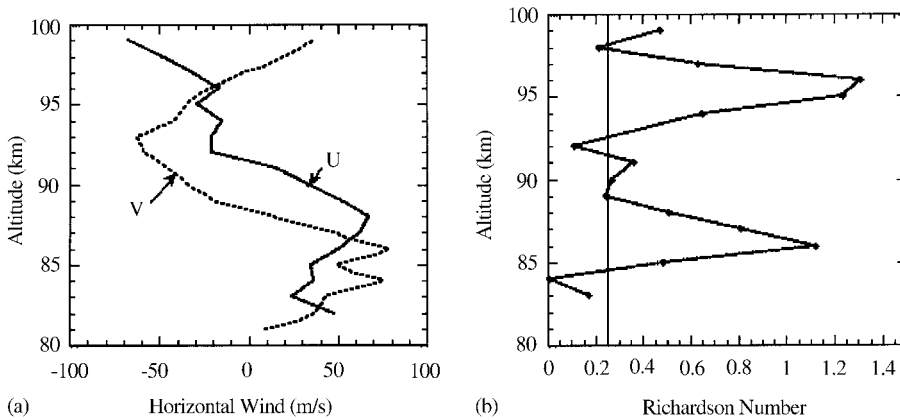

Fig. 7. (a) Horizontal wind and (b) Ri profiles at 0949 UT on 18 February 1999 with vertical resolution of 1 km. The straight vertical line in (b) is $Ri = \frac{1}{4}$, the critical value for dynamic instability. Left (right) of this line the air is dynamically unstable (stable).
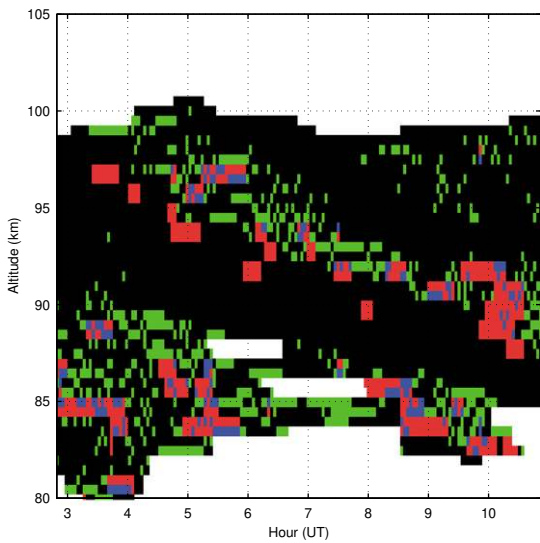

Fig. 8. Dynamically and convectively unstable regions based on Ri and N^2 for 18 February 1999. Black region are stable; red region are dynamically unstable ($0 < Ri < \frac{1}{4}$); green region are convectively unstable ($N^2 < 0$). No data is available in purple region.
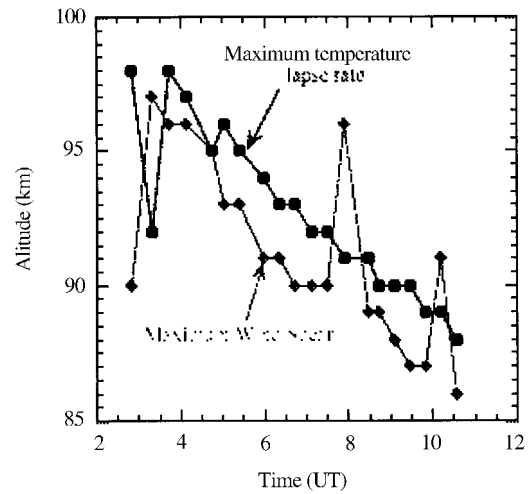

Fig. 9. Altitude of temperature shear maximum and total wind shear maximum versus time for the night of 18 February 1999.
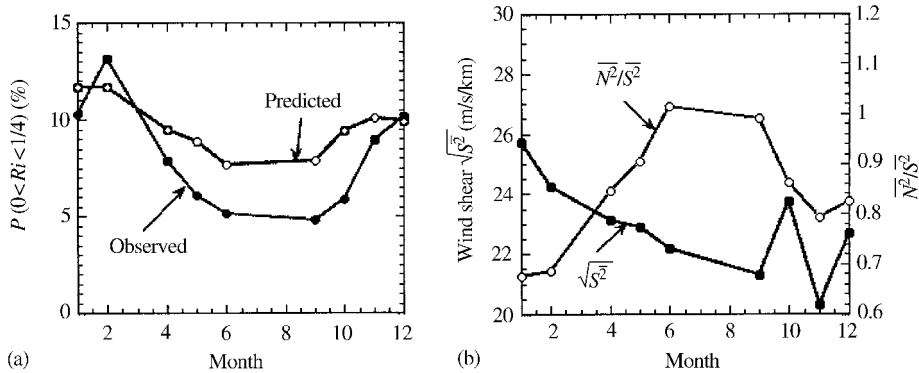
Fig. 10. (a) Monthly mean probability of dynamical instability $P(0 < Ri < \frac{1}{4})$ calculated using 1 km, 20 min resolution data. (b) Monthly mean total wind shear $\sqrt{\overline{S^2}}$ and $\overline{N^2/S^2}$ N^2/S^2.
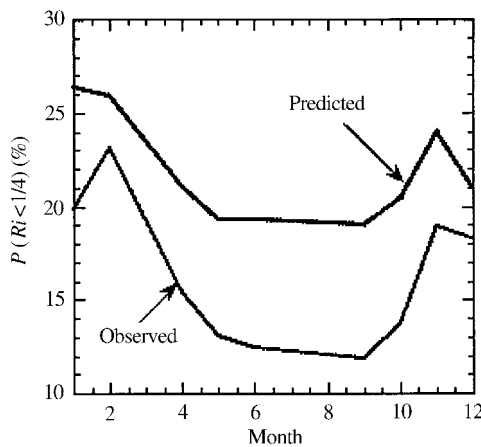

Fig. 11. Observed and predicted total probability of instability $P(Ri < \frac{1}{4})$.

smaller $\overline{S^2}$ in the summer. The mean value of the wind shear is maximum in January ($25.7 \text{ m s}^{-1} \text{ km}^{-1}$) and minimum in September ($22.1 \text{ m s}^{-1} \text{ km}^{-1}$). The mean value of Ri is considerably larger in summer (1.06) than in winter (0.68). For Ri to be less than $\frac{1}{4}$, the total wind shear must be larger than $2\sqrt{\overline{N^2}}$ or about $46 \text{ m s}^{-1} \text{ km}^{-1}$ in summer and $41 \text{ m s}^{-1} \text{ km}^{-1}$ in winter. These values are much larger than the monthly means, indicating that on average, the atmosphere is not likely to be dynamically unstable. The theoretical and measured probabilities of dynamic instability are in reasonable agreement except for August (not shown). This disagreement in August in probably a consequence of the small amount of data for this month. Only 10 h of measurements on two different nights were obtained in August.

The measured and theoretical total probabilities of instability $P(Ri < \frac{1}{4})$ are listed in Table 1 and their monthly means are plotted in Fig. 11. The annual mean $P(Ri < \frac{1}{4})$ is 15.5% with a maximum of 33% on 18 February 1999 and a minimum of 3.7% on 24 June 1998. The monthly mean total

probability of instability varies from a minimum of 12% in summer to a maximum of 23% in winter, and also shows a strong seasonal variation.

5. Summary and conclusions

The probabilities of static and dynamic instabilities are sensitive functions of $\overline{N^2/S^2}$, where N is the buoyancy frequency and S is the total vertical shear of horizontal winds. The upper mesosphere is most stable in summer when the mesopause is low, N is large and S is small. $\overline{N^2/S^2}$ varies from a maximum value of about 1.06 in mid-summer to a minimum of 0.68 in January. The probabilities of static and dynamic instabilities are maximum in mid-winter when they average about 10% and 12%, respectively, and minimum in summer, averaging 7% and 5%, respectively. The observations are generally consistent with theoretical predictions based on Gaussian models for the temperature and wind fluctuations induced by gravity waves. The observations also show that statically unstable conditions are generally preceded by dynamically unstable conditions.

The instability probabilities vary considerably from night to night. The structure of the unstable regions are significantly influenced by atmospheric tides. Tides alone are usually not strong enough to induce instability. However they can establish the environment for instabilities to develop. As the tidal temperature perturbations propagate downward, they reduce the stability on the topside of the temperature oscillation. Instabilities are then induced as gravity waves propagate through this layer of reduced static stability.

Appendix A. Analytical solutions

Because of the background temperature structure, static stability is usually maintained throughout the atmosphere in the absence of perturbing effects. However, in the middle atmosphere and especially in the mesopause region, temperature fluctuations associated with tides and gravity waves can induce instabilities. Because the wave induced temperature fluctuations are typically only a few percent or less, the perturbed stability parameter can be expressed approximately as

$$N^2 \approx \overline{N^2}(1 - T'/\bar{T}) + \frac{g}{\bar{T}} \frac{\partial T'}{\partial z}, \qquad (A.1)$$

where the overbar denotes the unperturbed quantities and T' is the temperature perturbation. Numerous waves from many different sources contribute to T' so that according to the central limit theorem, T' and hence N^2, are approximately. Gaussian distributed random processes (Gardner and Yang, 1998). The mean of N^2 is approximately $\overline{N^2}$ and the variance is

$$\text{var}(N^2) = \sigma_{N^2}^2 \approx (\overline{N^2})^2 \frac{\text{var}(T')}{\bar{T}^2} + \left(\frac{g}{\bar{T}}\right)^2 \text{var}\left(\frac{\partial T'}{\partial z}\right)$$

$$\approx \left(\frac{g}{\bar{T}}\right)^2 \text{var}\left(\frac{\partial T'}{\partial z}\right), \qquad (A.2)$$

where

$$\text{var}\left(\frac{\partial T'}{\partial z}\right) = \frac{1}{2\pi} \int_0^\infty m^2 F_T(m) \, dm, \qquad (A.3)$$

and $F_T(m)$ is the vertical wavenumber spectrum of the temperature fluctuations. The probability of static instability, $P(N^2 < 0)$, can be expressed in terms of the complementary error function.

$$P(N^2 < 0) = \int_{-\infty}^0 p(N^2) \, dN^2 = \frac{1}{2} \text{erfc}(\overline{N^2}/\sqrt{2}\sigma_{N^2}), \qquad (A.4)$$

where

$$p(N^2) = \frac{1}{\sqrt{2\pi}\sigma_{N^2}} \exp\left[-\frac{(N^2 - \overline{N^2})^2}{2\sigma_{N^2}^2}\right]. \qquad (A.5)$$

The probability of instability depends only on the ratio $\overline{N^2}/\sigma_{N^2} \approx (\partial\bar{T}/\partial z + g/C_p)/\text{std}(\partial T'/\partial z)$. It is small when $\overline{N^2} \propto (\partial\bar{T}/\partial z + g/C_p)$ is large and $\text{std}(N^2) = \sigma_{N^2} \propto \text{std}(\partial T'/\partial z)$ is small. In the absence of wave perturbations σ_{N^2} is zero and so is the probability of static instability. The probability approaches $\frac{1}{2}$ (i.e. 50%) as σ_{N^2} approaches infinity.

Our observations reported here show that the wave activity and stability of the background atmosphere vary seasonally. The mesopause region is most stable in summer when the mesopause is low (~ 86 km) and $\overline{N^2}$ is largest (see Fig. 6). The probability of static instability given by (A.4) is plotted versus $\overline{N^2}/\sigma_{N^2}$ in Fig. 12a. In this study the measured ratio $\overline{N^2}/\sigma_{N^2}$ varies between 0.87 and 1.55 with an annual mean of 1.17. For this range of $\overline{N^2}/\sigma_{N^2}$ values, the predicted probability of instability varies between about 6% and 20%.

The probability of dynamic instability can be estimated theoretically by making several reasonable assumptions about the temperature and wind fluctuations. First, we assume that the background wind shear is negligible compared to the large vertical shears in the horizontal winds induced by gravity waves and tides. We also assume that the wave field is approximately isotropic so that the mean square zonal and meridional wind perturbations and their vertical shear variances are equal. Analysis of the SOR dataset suggests that the wave field is approximately horizontally isotropic. The rms zonal and meridional wind perturbations average 20.4 and 20.5 m s^{-1}, respectively. Under these assumptions, the zonal and meridional shears are identically distributed zero mean Gaussian random processes and the total shear S is Rayleigh distributed

$$p(S) = \frac{2S}{\overline{S^2}} \exp(-S^2/\overline{S^2}), \qquad (A.6)$$

with a mean square value of

$$\overline{S^2} = \frac{1}{2\pi} \int_0^\infty m^2 F_{u+v}(m) \, dm, \qquad (A.7)$$

where $F_{u+v}(m)$ is the vertical wavenumber spectrum of the total horizontal wind fluctuations. When the wave field is isotropic there is no net horizontal transport of heat. In this case the horizontal heat fluxes ($\overline{u'T'}$ and $\overline{v'T'}$) are zero which implies that the Gaussian distributed temperature and horizontal wind perturbations are uncorrelated and hence, statistically independent. For the SOR dataset the horizontal heat flux magnitudes are typically no more than 10–20 km s^{-1}. The horizontal wind and temperature correlation coefficients are typically less than 0.1. Therefore, we assume N^2 is independent of S so that the probability of dynamic instability is given by

$$P(0 < Ri < \tfrac{1}{4}) = \int_0^\infty P\left(S^2 > 4N^2|N^2\right)_p \left(N^2\right) dN^2$$

$$= \exp\left[-\frac{4\overline{N^2}}{\overline{S^2}} + \left(\frac{4\sigma_{N^2}}{\sqrt{2}\overline{S^2}}\right)^2\right]$$

$$\times \left[1 - \frac{1}{2}\text{erfc}\left(\frac{\overline{N^2}}{\sqrt{2}\sigma_{N^2}} - \frac{4\sigma_{N^2}}{\sqrt{2}\overline{S^2}}\right)\right]$$
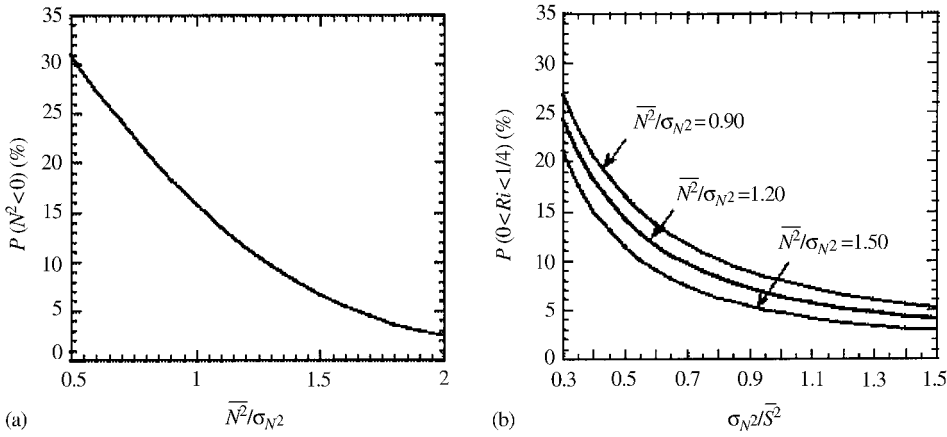
Fig. 12. Predicted probabilities of (a) convective instability $P(N^2 < 0)$ versus $\overline{N^2}/\sigma_{N^2}$ and (b) dynamic instability $P(0 < Ri < \frac{1}{4})$ versus $\sigma_{N^2}/\overline{S^2}$ with different value of $\overline{N^2}/\sigma_{N^2}$.

$$= \frac{1}{2} \exp\left[-\frac{4\overline{N^2}}{\overline{S^2}} + \left(\frac{4\sigma_{N^2}}{\sqrt{2\overline{S^2}}} \right)^2 \right]$$

$$\times \mathrm{erfc}\left(\frac{4\sigma_{N^2}}{\sqrt{2\overline{S^2}}} - \frac{\overline{N^2}}{\sqrt{2}\sigma_{N^2}} \right), \qquad (A.8)$$

where $p\left(N^2\right)$ is given by (A.5) and

$$P(S^2 > 4N^2 | N^2) = \int_{2N}^{\infty} p(s)\,\mathrm{d}s = \exp(-4N^2/\overline{S^2}). \quad (A.9)$$

The probability of dynamic instability is a function of the ratios $\overline{N^2}/\sigma_{N^2}$ and $\sigma_{N^2}/\overline{S^2}$. It approaches $\exp(-4\overline{N^2}/\overline{S^2})$ as σ_{N^2} approaches zero and becomes zero when σ_{N^2} approaches infinity.

The probability of dynamic instability given by (A.8) is plotted in Fig. 12b versus $\sigma_{N^2}/\overline{S^2}$ for several values of $\overline{N^2}/\sigma_{N^2}$. In this study the measured values of $\overline{S^2}$ vary between $(16.3 \text{ m s}^{-1}\text{ km}^{-1})^2$ and $(29.8 \text{ m s}^{-1}\text{ km}^{-1})^2$ with a mean value of $(23.0 \text{ m s}^{-1}\text{ km}^{-1})^2$. The measured ratios $\sigma_{N^2}/\overline{S^2}$ vary between 0.46 and 1.46 with a mean value of 0.72. For this range of $\sigma_{N^2}/\overline{S^2}$ values, the theoretical probability of dynamic instability varies between about 4% and 16%. The effects of the temperature perturbations on dynamic instability can be assessed by comparing the probabilities predicted by Eq. (A.9) with the limit for $\sigma_{N^2} = 0$. By using the mean observed values for $\overline{N^2}$, σ_{N^2} and $\overline{S^2}$, the limiting probability in the absence of temperature fluctuations is $\exp(-4\overline{N^2}/\overline{S^2}) = 3.5\%$ while Eq. (A.8) predicts 9.5%.

The relationship between gravity wave horizontal wind and temperature perturbations is given by the polarization relations. For waves with intrinsic periods much less than the inertial period (~ 21 h at SOR), the relationships can be expressed as (Hines, 1974)

$$\mathrm{var}(u') + \mathrm{var}(v') \approx \frac{g^2}{\overline{N^2}} \frac{\mathrm{var}(T)}{\bar{T}^2}, \qquad (A.10)$$

$$\overline{S^2} \approx \frac{g^2}{\overline{N^2}} \frac{\mathrm{var}(\partial T'/\partial z)}{\bar{T}^2}, \qquad (A.11)$$

so that

$$\overline{N^2}/\sigma_{N^2} \approx \sigma_{N^2}/\overline{S^2} \approx \sqrt{\overline{N^2/S^2}}. \qquad (A.12)$$

By substituting Eq. (A.12) into Eq. (A.4) and Eq. (A.8) we obtain

$$P(\overline{N^2} < 0) \approx \frac{1}{2}\,\mathrm{erfc}(\sqrt{\overline{N^2/2S^2}}), \qquad (A.13)$$

$$P(0 < Ri < \tfrac{1}{4}) \approx \frac{1}{2}\exp(4\overline{N^2/S^2})$$

$$\times \mathrm{erfc}(3\sqrt{\overline{N^2/2S^2}}). \qquad (A.14)$$

For pure gravity wave perturbations, both probabilities can be expressed as functions of the single ratio $\overline{N^2/S^2}$. The total probability of instability, $P(Ri < \frac{1}{4})$, is just the sum of the probabilities of static and dynamic instabilities. $P(N^2 < 0), P(0 < Ri < \frac{1}{4})$, and $P(Ri < \frac{1}{4})$ given by Eqs. (A.13) and (A.14) are plotted versus $\overline{N^2/S^2}$ in Fig. 13. For pure gravity wave perturbations, static instabilities are more probable than dynamic instabilities. We emphasize that all these formulas for the instability probabilities (Eqs. (A.4), (A.8), (A.13), and (A.14)) are approximate and were derived to facilitate interpretation of the observations reported here. The presence of large amplitude gravity waves and tides during a given observation period, can alter substantially the statistics of the wind and temperature fluctuations, the instability probabilities, and the structure of the unstable regions.

Appendix B. Bias correction

The Na wind/temperature lidar technique is technically mature (Bills et al., 1991; Bills and Gardner, 1993; She et al., 1992; Papen et al., 1995; Yu et al., 1996) and the measurement errors are dominated by photon noise. The
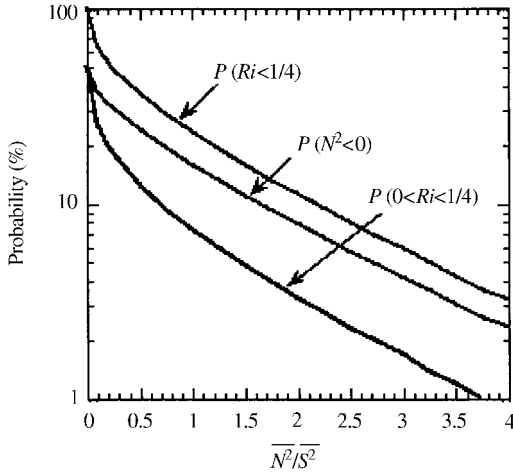
Fig. 13. Predicted probability of convective instability $P(N^2 < 0)$, dynamic instability $P(0 < Ri < \frac{1}{4})$ and total instability $P(Ri < \frac{1}{4})$ versus $\overline{N^2}/\overline{S^2}$.

measured temperature can be written as

$$T = \bar{T} + T' + \Delta T, \tag{B.1}$$

where $\bar{T}$ is the background atmospheric temperature in the absence of wave perturbations, T' is the wave perturbation, and ΔT is the error caused by photon noise. T' and ΔT are statistically independent and both are approximately Gaussian distributed zero mean random processes. Since ΔT is small compared to $\bar{T}$, the measurement error for the stability parameter N^2 is given by

$$\Delta N^2 \approx \frac{g}{\bar{T}} \frac{\partial \Delta T}{\partial z} - \overline{N^2} \frac{\Delta T}{\bar{T}}. \tag{B.2}$$

The photon noise increases the variance of the measured stability parameter,

$$\mathrm{var}(N^2 + \Delta N^2) = \sigma_{N^2}^2 + \mathrm{var}(\Delta N^2), \tag{B.3}$$

where

$$\mathrm{var}(\Delta N^2) = \left[(\overline{N^2})^2 + 2 \left(\frac{g}{\Delta z} \right)^2 \right] \frac{\mathrm{var}(\Delta T)}{\bar{T}^2}$$

$$\approx 2 \left(\frac{g}{\Delta z} \right)^2 \frac{\mathrm{var}(\Delta T)}{\bar{T}^2}. \tag{B.4}$$

The factor 2 comes from the fact that the vertical derivative is calculated by differencing T at two adjacent altitudes. The second term in the bracket is much larger that the first term (by at least 3 orders of magnitude). $\mathrm{var}(\Delta T)$ can be estimated from the raw lidar photon count profiles. For the data reported here, the rms temperature error averages less than 1.5 K so that the rms error in N^2 is less than about 2×10^{-4} s^{-2}.

If the measurement errors are small, the measured probability of static instability can be expressed as

$$P(N^2 + \Delta N^2 < 0) \approx P(N^2 < 0)$$

$$+ \Delta P \left[\overline{N^2}, \sigma_{N^2}^2, \mathrm{var}(\Delta N^2) \right], \tag{B.5}$$

where

$$\Delta P[\overline{N^2}, \sigma_{N^2}^2, \mathrm{var}(\Delta N^2)]$$

$$= \mathrm{var}(\Delta N^2) \frac{\partial P(N^2 < 0)}{\partial \sigma_{N^2}^2} \bigg|_{\sigma_{N^2}^2}$$

$$= \mathrm{var}(\Delta N^2) \int_{-\infty}^0 \frac{\mathrm{e}^{-(N^2 - \overline{N^2})^2 / 2\sigma_{N^2}^2}}{2\sigma_{N^2}^3 \sqrt{2\pi}}$$

$$\times \left[\frac{(N^2 - \overline{N^2})^2}{\sigma_{N^2}^2} - 1 \right] \mathrm{d}N^2$$

$$= \mathrm{var}(\Delta N^2) \frac{\overline{N^2}}{2\sqrt{2\pi}\sigma_{N^2}^3} \mathrm{e}^{-(\overline{N^2})^2 / 2\sigma_{N^2}^2}. \tag{B.6}$$

The bias in the measured probability of instability, ΔP, can be estimated using Eq. (B.6) and the measured values of $\overline{N^2}, \mathrm{var}(\Delta N^2)$ and $\mathrm{var}(N^2 + \Delta N^2)$. The reported static instability probabilities are computed by measuring the relative frequency of instability for each night of observations and subtracting the bias predicted by Eq. (B.6).

The accuracy of the bias correction depends on the accuracy of the measured and computed values of $\overline{N^2}$, $\sigma_{N^2}^2$ and $\mathrm{var}(\Delta N^2)$. The error in the bias term associated with errors in these parameters can be estimated by taking the derivative of Eq. (B.6) with respect to each parameter and multiplying the result by the corresponding estimated parameter error.

To verify this technique, the measured and corrected probabilities of static instability for the night of 12 January 1999 were computed with several different temperature error cutoff values. Only temperature data with errors less than the cutoff value were used to compute N^2 and to determine the regions of static instability. The results are shown in Fig. 14. The horizontal axis is the temperature error cutoff value. As the temperature error cutoff value increases, the measured probability of instability increases because $\mathrm{var}(\Delta N^2)$ increases. However, the compensated probability of instability remains relatively constant, indicating that the compensation procedure is effective in removing the bias associated with the temperature errors. Notice that the uncertainty of the compensated probability increases as the temperature error cutoff value increases. For all the data reported here, a cutoff value of 2.5 K were used. The uncertainties in the compensated probabilities in Table 1 were estimated using Eq. (B.6) with the estimated uncertainties of $\overline{N^2}$, $\sigma_{N^2}^2$ and $\mathrm{var}(\Delta N^2)$.

Even though the uncertainty of N^2 calculated in each individual sample is relative large, the probability of instability
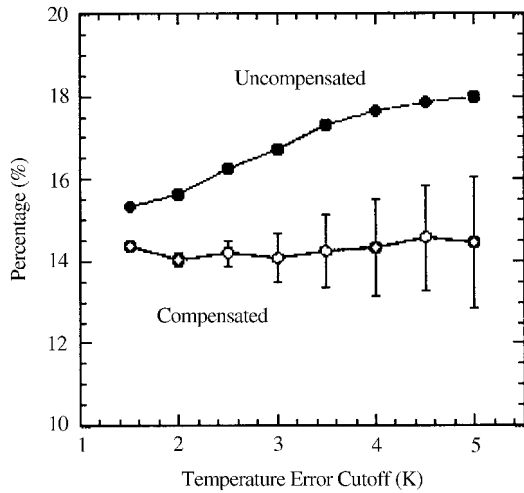
Fig. 14. Probability of convective instability calculated with different temperature error criteria for 12 January 1999. Solid circles represent uncompensated probability $P(N^2 + \Delta N^2 < 0)$; open circles represent compensated probability $P(N^2 < 0)$. Error bars are also plotted for the compensated probability.

Fig. 16. Histograms of $P(N^2 < 0)$ on 12 Jan, 1999 based on 5000 Monte-Carlo simulations.

temperature, and then calculating N^2 and $P(N^2 < 0)$ with the added noise. The standard deviation of the added random noise is set to the known temperature error in the measured temperature profiles. After many repetitions, a distribution of $\overline{N^2}$ and $P(N^2 < 0)$ can be obtained. The standard deviation of $P(N^2 < 0)$ is a numerical estimate of its uncertainty associated with the temperature error.

The simulation was performed with the data on the night of 12 January 1999. Fig. 15 is the histogram of N^2 with and without random errors from one sample run. Notice that by adding random errors, the distribution of N^2 is broadened, resulting in relatively more negative samples of $N^2 + \Delta N^2$, and therefore $P(N^2 + \Delta N < 0)$ increased from 16.3% to 20.6%. As predicted by the analytical solutions (B.6), an increase in var(ΔN^2) will always give a positive bias in the measured instability probability.

Fig. 16 is the distribution of $P(N^2 + \Delta N^2 < 0)$ from 5000 runs. This distribution is very narrow. Its standard deviation is 0.35%, close to the value estimated from analytical calculation (0.33% in the first data row in Table 1). This result demonstrates that the probability of instability can be reliably estimated with the given temperature uncertainty, and the analytical estimate of the uncertainty is a good approximation to the actual uncertainty.
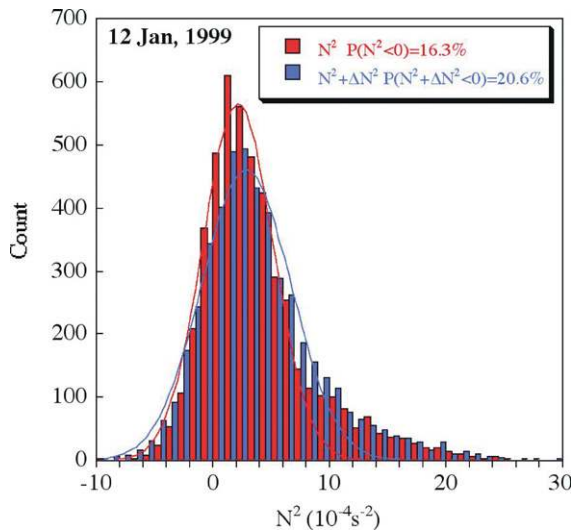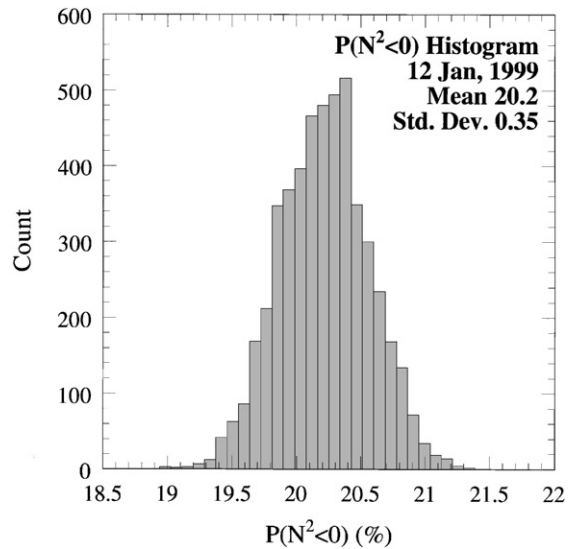

Fig. 15. Histograms of N^2 and $N^2 + \Delta N^2$ on 12 Jan, 1999 from Monte-Carlo simulation. $N^2 + \Delta N^2$ is generated by adding Gaussian distributed random errors to the temperature. The standard deviation of the random errors is set to be the same as to the temperature uncertainty. The curves are Gaussian best fits for the two distributions.

has a relatively small uncertainty because it is a statistic of N^2 for a large number of samples. This uncertainty can be estimated from analytical solutions shown above. To further verify this, we use Monte-Carlo simulation to numerically calculate this uncertainty. The Monte-Carlo experiment is done by adding Gaussian distributed random noise to the

References

Allen, S.J., Vincent, R.A., 1995. Gravity wave activity in the lower atmosphere: Seasonal and latitudinal variations. Journal of Geophysical Research 100, 1327–1350.

Bills, R.E., Gardner, C.S., 1993. Lidar observations of the mesopause region temperature structure at Urbana. Journal of Geophysical Research 98, 1011–1021.

Bills, R.E., Gardner, C.S., She, C.Y., 1991. Narrowband lidar technique for sodium temperature and Doppler wind observations of the upper atmosphere. Optical Engineering 30, 13–21.

Blix, T.A., Thrane, E.V., Fritts, D.C., von Zahn, U., Lübken, F.-J., Hillert, W., Blood, S.P., Mitchell, J.D., Kokin, G.A., Pakhomov, S.V., 1990. Small-scale structure observed in-situ during MAC/EPSILON. Journal of Atmospheric and Terrestrial Physics 52, 835–854.

Dewan, E.M., Good, R.E., 1986. Saturation and the "universal" spectrum for vertical profiles of horizontal scalar winds in the atmosphere. Journal of Geophysical Research 91, 2742–2748.

Dunkerton, T.J., 1987. Effect of nonlinear instability on gravity wave momentum transport. Journal of Atmospheric Science 44, 3088–3209.

Emanuel, K.A., 1994. Atmospheric Convection, Oxford University Press, New York, 580pp.

Fritts, D.C., Isler, J.R., Andreassen, Ø., 1994. Gravity wave breaking in two and three dimensions, 2, Three-dimensional evolution and instability structure. Journal of Geophysical Research 99, 8109–8123.

Gardner, C.S., 1994. Diffusive filtering theory of gravity wave spectra in the atmosphere. Journal of Geophysical Research 99, 20,601–20,622.

Gardner, C.S., Yang, W., 1998. Measurements of the dynamical cooling rate associated with the vertical transport of heat by dissipating gravity waves in the mesopause region at the Starfire Optical Range, New Mexico. Journal of Geophysical Research 103, 16,909–16,926.

Hines, C.O., 1974. The Upper Atmosphere in Motion, Geophysical Monograph Series, Vol. 18, AGU, Washington, DC, p. 426.

Hines, C.O., 1991. The saturation of gravity waves in the middle atmosphere. II. Development of Doppler-spread theory. Journal of Atmospheric Science 48, 1360–1379.

Hodges Jr., R.R., 1967. Generation of turbulence in the upper atmosphere by internal gravity waves. Journal of Geophysical Research 72, 3455–3458.

Koop, C.G., McGee, B., 1986. Measurements of internal gravity waves in a continuously stratified shear flow. Journal of Fluid Mechanics 172, 453.

Kundu, Pijush, K., 1990. Fluid Mechanics, Academic Press, San Diego, 638pp.

Lindzen, R.S., 1981. Turbulence and stress owing to gravity wave and tidal breakdown. Journal of Geophysical Research 86, 9707–9714.

Lübken, F.-J., Hillert, W., Lehmacher, G., von Zahn, U., Blix, T.A., Thrane, E.V., Widdel, H.-U., Kokin, G.A., Knayazev, A.K., 1994. Morphology and sources of turbulence in the mesosphere during DYANA. Journal of Atmospheric and Terrestrial Physics 56, 1809–1833.

Offermann, D., 1994. The DYANA campaign: a survey. Journal of Atmospheric and Terrestrial Physics 56, 1639–1657.

Papen, G.C., Gardner, C.S., Pfenninger, W.M., 1995. Analysis of a potassium lidar system for upper-atmospheric wind-temperature measurements. Applied Optics 34, 6950–6958.

Pfenninger, M.A., Liu, A.Z., Papen, G.C., Gardner, C.S., 1999. Gravity wave characteristics in the lower atmosphere at south pole. Journal of Geophysical Research 104, 5963–5984.

Rohr, J.J., Itsweire, E.E., Helland, K.N., VanAtta, C.W., 1988. Growth and decay of turbulence in a stably stratified shear flow. Journal of Fluid Mechanics 193, 77–111.

She, C.Y., Yu, J.R., Latifi, H., Bills, R.E., 1992. High-spectral-resolution lidar for mesospheric sodium temperature measurements. Applied Optics 31, 2095–2106.

Sica, R.J., Thorsley, M.D., 1996. Measurements of superadiabatic lapse rates in the middle atmosphere. Geophysical Research Letters 23, 2797–2800.

States, R.J., Gardner, C.S., 2000. Thermal structure of the mesopause region (80–105 km) at $40°$ N latitude Part II: Diurnal variations. Journal of Atmospheric Science 57, 66–77.

Weinstock, J., 1990. Saturated and unsaturated spectra of gravity waves and scale-dependent diffusion. Journal of Atmospheric Science 47, 2211–2225.

Yu, J.R., Yang, W., Gardner, C.S., 1996. A Novel Acousto-Optic Modulation Technique for Na Wind/Temperature Lidars. Advances in Atmospheric Remote Sensing with Lidar, Selected Papers of the 18th International Laser Radar Conference, Berlin, 22–26 July 1996, Springer-Verlag, Heidelberg, Germany, pp. 573–576.